

Ultrafast Inverse Design of Electromagnetic Devices

Yifei Zheng[†], Mohamed Elsayaf[†], Jui-Hung Sun[†], Ho-Chun Lin,
Chia Wei Hsu, Constantine Sideris*

Ming Hsieh Department of Electrical Engineering, University of Southern
California, 3740 McClintock Ave, Los Angeles, 90089, California, USA.

*Corresponding author(s). E-mail(s): csideris@usc.edu;
Contributing authors: yzheng@usc.edu; elsawaf@usc.edu;
juihangs@usc.edu; hochunli@usc.edu; cwhsu@usc.edu;

[†]These authors contributed equally to this work.

Abstract

This paper introduces the Precomputed Numerical Green Function (PNGF) method, a new approach for rapid inverse design of electromagnetic devices. The static components of the design are incorporated into a numerical Green function obtained from a single fully parallelized precomputation step, reducing the cost of evaluating candidate designs during optimization to only being proportional to the size of the region under modification. When used with the direct binary search optimization algorithm, a low-rank update technique is leveraged to further decrease the iteration time to seconds without approximations or compromises in accuracy. The total runtime for an inverse design is reduced by several orders of magnitude compared to using conventional Maxwell solvers due to the linear time complexity of the method, attaining speedups of up to 700x for the design examples considered and lowering the process from multiple days to weeks down to less than an hour. The performance and flexibility of the approach are highlighted with design studies, including experimental results, on an ultrawideband 30GHz substrate antenna with 50% fractional bandwidth, a 6GHz switched-beam antenna steerable between angles 90° apart, and a broadband, ultra-short-length microstrip to substrate-integrated waveguide transition. The approach stands to reshape inverse design in electromagnetics.

Keywords: Inverse design, numerical Green function, direct binary search, finite-difference, augmented partial factorization, Woodbury identity, reconfigurable antenna, substrate-integrated waveguide

1 Main

Electromagnetic devices are an indispensable part of daily life, playing key roles in telecommunications, radar, sensors, biomedical devices, and more. The conventional process of electromagnetic design is heavily reliant on human intuition and experience, and the iterative nature of design is time-consuming and resource-intensive. As such, inverse design techniques —algorithmic approaches for the discovery and optimization of devices or structures yielding desired functional properties —have attracted significant focus across many disciplines, including RF/mm-wave [1–13], nanophotonics and optics [14–22], and materials and structural engineering [23–27]. The properties of interest are encoded as objective functions that are extremized via optimization methods. The paradigm of inverse design is appealing owing to its capability for broad exploration of design spaces with many degrees of freedom, enabling the synthesis of novel devices achieving performance superior to that of conventional designs.

In gradient-based inverse design approaches, optimization is performed by iteratively following the gradient of the objective function computed over the space of input parameters. Such methods are liable to converge to local extrema, and many inverse design runs at random starting configurations may be required before satisfactory results are attained. Moreover, a gradient may not be available due to discrete-valued input parameters, such as metal conductivities and substrate dielectric constants; allowing such parameters to vary continuously may result in physically infeasible designs. As a result, gradient-free optimization approaches, such as genetic algorithms [1, 2, 14] and particle swarm optimization [3–5, 28], have been introduced, enabling wider design space coverage. However, a prominent limitation of both gradient-based and gradient-free techniques for electromagnetic design is that full-wave field simulations are required to evaluate the objective function at each optimization iteration. Even with the fastest commercially-available solvers, such as Ansys HFSS or CST Studio, single simulations often take tens of minutes to hours to run even for structures of only moderate complexity.

As such, objective function evaluation is typically the rate-limiting factor for design throughput, and mitigating this has been the subject of much work. For instance, adjoint methods [6, 15, 16] for gradient-based approaches allow the gradient to be computed with only two field simulations per iteration. Alternatively, to dispense with simulation entirely during optimization, machine-learning techniques, which construct surrogate models that allow performance to be predicted from the input parameters, have garnered widespread attention within and beyond electromagnetic design [7–9, 11–13, 17, 19, 22, 24–26]. While neural-network surrogates can greatly reduce optimization time, the process is constrained by computationally-expensive training as well as the large number of simulations needed for adequate design space coverage when generating training datasets. Although approaches such as transfer learning have been introduced to enhance training efficiency, the training phase, inclusive of the generation of the large dataset (on the order of 10,000 to > 1 million simulations [7, 9, 11, 17, 26]), may nonetheless require multiple days to weeks [8, 11, 13, 22]. Furthermore, over the full design space, there is no guarantee of accuracy given valid input parameters [22, 29]; that is, a design predicted as optimal by the surrogate

may yield completely different performance when verified with full-wave simulation or measurement of a fabricated device.

This paper introduces an approach for inverse design of electromagnetic devices with rapid, direct, approximation-free objective function evaluation at each optimization iteration. While pixelated metallic structures and the direct binary search (DBS) global optimization problem are the focus of this work, the method can be generalized to dielectric optimization problems and can also be used with other optimization approaches. Pixels or tiles in the simulation environment are replaced with equivalent electric current densities, allowing the interaction between the static, unchanging portions of the device and the dynamic optimization region to be represented by a numerical Green function matrix obtained from a single fully parallelized precomputation step. During optimization, the objective function may be obtained by solving a linear system whose number of unknowns is equal to only the size of the optimization region. Additionally, since DBS modifies only one tile per iteration, a low-rank update method can be utilized to accelerate evaluation speed significantly without trade-offs in accuracy. The cost of evaluation is linear with the size of the optimization region, which reduces the total runtime of the full inverse design by several orders of magnitude from several days or weeks (with commercial solvers) to minutes. Unlike neural network-based surrogate models, this method yields a highly-accurate solution, which matches those obtained from the full-wave electromagnetic solver leveraged for pre-computation to machine precision and is correct for every design in the feasible set, without training.

The PNGF method is applied to design three example devices: an ultrawideband 30GHz substrate antenna with 50% fractional bandwidth, a 6GHz planar switched-beam antenna (SBA) whose beam is switchable over a 90° angle, and a broadband short-length transition between a microstrip feedline and a substrate-integrated waveguide (SIW). When PNGF is utilized as the solver for DBS, speedups of up to 700x in the optimization time versus DBS using the fastest commercial software (e.g., HFSS and CST) are obtained, establishing a new standard of performance. The SBA and microstrip-SIW transition are fabricated, and the measured scattering parameters of the devices and the radiation pattern of the SBA agree closely with predicted simulation results.

2 Numerical Green's functions

A pixelated electromagnetic structure, such as the example shown in Fig. 1(a), encompasses a predefined optimization region comprising tiles, each of which may be filled with metal, or left open (i.e., filled with the dielectric material of the substrate). The goal of design is to find a configuration of tiles that yields desired electromagnetic properties. Additional components of the device, such as dielectric structures, ground planes, feedlines, and air gaps, are constrained to be static and are excluded from being modified during optimization. To model the structure, 3D space is discretized into a grid of voxels (typically by using a finite-difference or finite-element algorithm) in a simulation environment, as illustrated in Fig. 1(b). Usually, each tile comprises a rectangular array of several voxels in length and width. Finite-difference methods are

leveraged in this work, where each voxel is a cell in the finite-difference Yee lattice [30]. However, any solution method, such as finite-element methods (FEM) or boundary element methods (BEM), can be used instead.

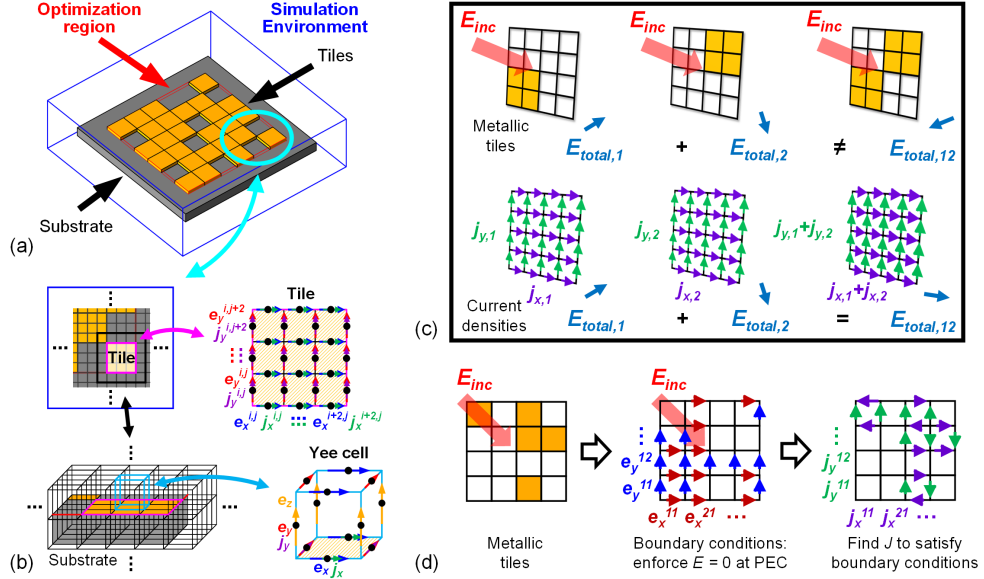


Fig. 1: Current equivalence for pixelated electromagnetic devices. (a) Representative pixelated electromagnetic structure; (b) Example discretization of simulation environment with planar optimization region, where each voxel is a finite-difference Yee cell and each tile comprises the faces of 3×3 cells; (c) Additivity of current densities, in contrast with metallic tiles; (d) Process to replace an arbitrary arrangement of metallic tiles with equivalent current densities that satisfy boundary conditions and produce identical fields. For simplicity, tiles in (d) are shown as comprising one voxel each, but in practice, multiple voxels constitute a tile.

Each optimization iteration would be significantly accelerated if candidate designs could be assessed via a linear combination of precomputed solutions to simpler designs, such as single tiles in an otherwise empty optimization region. However, as illustrated in Fig. 1(c), such solutions do not obey superposition since electromagnetic fields scatter from metals. As such, traditional approaches have required field simulations to evaluate the entire environment, including the static components, from scratch at each iteration. To overcome this limitation, we can apply the current equivalence theorem to represent any given configuration of the optimization region with polarization current densities, which create fields identical to those that would be generated by the original metallic structure in response to an excitation source, as illustrated in Fig. 1(d). The static components of the design are encoded into a numerical Green function matrix G that maps equivalent current densities to electric fields in the optimization region.

We seek to find an effective polarization density $\mathbf{J}_{\mathbf{p}}(\mathbf{r}) = \epsilon_0(\epsilon_r(\mathbf{r}) - 1)\mathbf{E}(\mathbf{r})$ where ϵ_0 is the free-space permittivity and $\epsilon_r(\mathbf{r})$ is the material permittivity, such that the fields \mathbf{E} produced by $\mathbf{J}_{\mathbf{p}}$ in an empty optimization region are identical to those with the metal tiles in response to an excitation \mathbf{E}_{inc} . The conductivity $\sigma(\mathbf{r})$ at points \mathbf{r} throughout the optimization region is either zero (free space) or infinity (metal represented by perfect electrical conductor (PEC)). Note that although we only consider PEC materials in our optimization region in this work, the method can be used with any arbitrary complex $\epsilon_r(\mathbf{r})$. Defining an auxiliary quantity $p(\mathbf{r})$ such that $\sigma(\mathbf{r}) = \frac{p(\mathbf{r})}{1-p(\mathbf{r})}$, it can be shown (see Supplementary Note SN.1) using the electric field volume integral equation [31] that

$$p(\mathbf{r})\mathbf{E}_{\text{inc}} = (1 - p(\mathbf{r}))\mathbf{J}_{\mathbf{p}}(\mathbf{r}) + p(\mathbf{r}) \int_V \overline{\overline{G_0}}(\mathbf{r}, \mathbf{r}')\mathbf{J}_{\mathbf{p}}(\mathbf{r}') dV', \quad (1)$$

where $\overline{\overline{G_0}}$ is the dyadic free space Green's function, $p(\mathbf{r}) = 1$ in the domain V corresponds to metal, and $p(\mathbf{r}) = 0$ corresponds to free space. The solution $\mathbf{J}_{\mathbf{p}}$ is unique and results in zero tangential electric field wherever there is metal, satisfying the PEC boundary conditions.

Equation (1) is strictly valid when the design comprises only metallic tiles and vacuum, as it uses the dyadic free-space Green's function. However, $\overline{\overline{G_0}}$ may be replaced with the Green's function for any particular simulation environment. While closed-form analytical Green's functions are usually not available, it is known that a Green's function exists for every linear system. To solve for the current density numerically for a given design under consideration, by choosing a suitable basis $\mathbf{J}_{\mathbf{p}}$ (e.g., piecewise constant) and testing functions [32], equation (1) can be discretized into

$$[(I - P) + PG]\mathbf{j} = C\mathbf{j} = P\mathbf{e}_{\text{inc}}, \quad (2)$$

where \mathbf{j} and \mathbf{e}_{inc} are the discretized polarization density and incident electric field vectors over the optimization region, and the design is encoded in P , a diagonal matrix whose entries indicate metal (1) or an empty tile (0). The vector indices correspond to the field components over discretized space (e.g. on the edges of Yee cells). The matrix G , a discretized form of the Green's function integral operator, needs only to be precomputed once for a given simulation environment, and then any candidate design may be evaluated by solving the linear system of equations (2) over only the optimization region, as illustrated in Fig. 2(a). The number of unknowns is the number of field components N_{opt} in the optimization region, which is considerably smaller than the number of unknowns N_{sim} comprising the full simulation environment. This involves no approximations and incurs no loss of accuracy compared to a conventional simulation of the full system.

3 Precomputation

In general, an electromagnetic field solver finds the inverse of a matrix A that satisfies $A\mathbf{e}_{\text{sim}} = \mathbf{j}_{\text{sim}}$, where the electric fields \mathbf{e}_{sim} and currents \mathbf{j}_{sim} encompass the entire

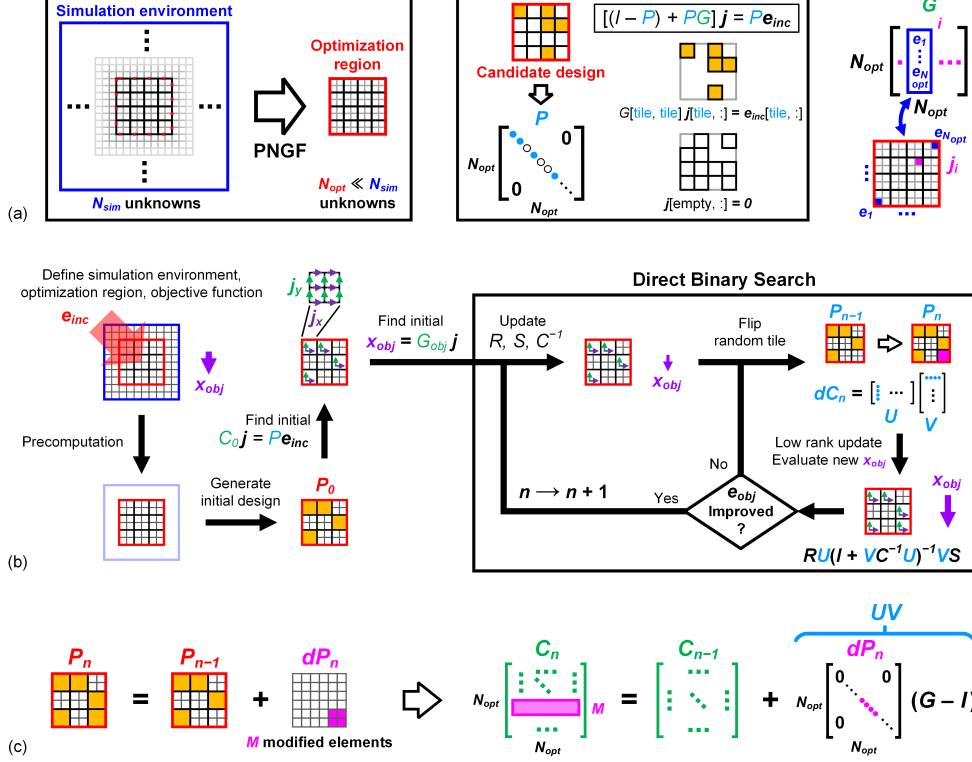


Fig. 2: Precomputed numerical Green function optimization with direct binary search. (a) Numerical Green function matrix G allowing candidate designs P to be evaluated by solving a linear system of only N_{opt} unknowns; (b) Process of direct binary search optimization with the PNGF method; (c) Tile flip yielding a low-rank update to the PNGF system matrix, which is performed with the Woodbury matrix identity in this work. For simplicity, tiles are shown as comprising 2×2 voxels each, whereas tiles generally encompass more voxels in practice.

simulation environment. A corresponds to the discretized Maxwell operator (in this work, the finite-difference frequency-domain matrix) of the simulation domain, comprising the static region and an empty optimization region. However, to obviate the need to compute the full A^{-1} , a tall logical $0-1$ projection matrix B may be defined to map vectors \mathbf{e}_{opt} and \mathbf{j}_{opt} in the optimization region to the corresponding vectors in the full simulation environment; that is, $\mathbf{e}_{opt} = B^T \mathbf{e}_{sim}$ and $\mathbf{j}_{sim} = B \mathbf{j}_{opt}$, where $B^T B = I$. As such,

$$\mathbf{e}_{opt} = B^T A^{-1} B \mathbf{j}_{opt}, \quad (3)$$

which has N_{opt} unknowns. The matrix $B^T A^{-1} B$ corresponds to G in equation (2) discretized using finite-differences, mapping currents \mathbf{j}_{opt} to fields \mathbf{e}_{opt} in the optimization region.

An iterative solver may be used to obtain G column-by-column, where each simulation yields the fields due to a current density at a single discretized spatial location in the optimization region. The N_{opt} simulations are linearly independent and as such may be run in parallel across many nodes. Additionally, time-domain methods such as finite-difference time-domain (FDTD) may be used, where the frequency-domain information in G is obtained from discrete Fourier transforms after each simulation. This allows a G matrix to be obtained at multiple frequencies per simulation for multi-frequency optimization.

Alternatively, a sparse direct solver may be used with a frequency-domain formulation to obtain G efficiently in a single shot with the recently-introduced augmented partial factorization (APF) technique [33]. The full system matrix A is constructed using the finite-difference frequency-domain (FDFD) formulation (see Supplementary Note SN.2). Then, an augmented sparse matrix K is set up such that A comprises the upper left block. K can be partially factorized as

$$K = \begin{bmatrix} A & B \\ B^T & 0 \end{bmatrix} = \begin{bmatrix} L & 0 \\ E & I \end{bmatrix} \begin{bmatrix} U & F \\ 0 & H \end{bmatrix}, \quad (4)$$

where L and U are the LU-factors and E and F are additional matrices not used for precomputation. The matrix H , known as the Schur complement [34], is given by $H = -B^T A^{-1} B$. Thus, G is obtained as $-H$, avoiding the need to apply the LU factors for A to find $B^T A^{-1} B$.

Field quantities outside the optimization region are often required to evaluate the objective function. A vector \mathbf{x}_{obj} of quantities needed for evaluation may be defined, and a matrix G_{obj} that maps current densities in the optimization region to \mathbf{x}_{obj} may be precomputed and utilized in optimization together with G . Each of the N_{obj} elements of \mathbf{x}_{obj} is a field value or a linear combination of field values. In practical scenarios, N_{obj} is rarely significantly larger than 1; for example, to compute a scalar mode amplitude with a discrete mode overlap integral, \mathbf{x}_{obj} would have $N_{obj} = 1$ element that is a linear combination of the fields at the evaluation points [35], and for a near-field to far-field transformation, two linear combinations are needed [30], giving $N_{obj} = 2$. A wide logical 0 – 1 projection matrix W^T may be defined to obtain \mathbf{x}_{obj} from the full simulation environment solution $\mathbf{e}_{sim} = A^{-1} B \mathbf{j}_{opt}$:

$$\mathbf{x}_{obj} = W^T A^{-1} B \mathbf{j}_{opt} = G_{obj} \mathbf{j}_{opt}. \quad (5)$$

Using the above methods, G_{obj} may be precomputed together with G directly without any additional computational cost. With an iterative solver, the number of excitations to be solved is still N_{opt} , since G_{obj} has N_{opt} columns. If APF is employed, the augmented system becomes

$$K_{obj} = \begin{bmatrix} A & B \\ \begin{bmatrix} B^T \\ W^T \end{bmatrix} & 0 \end{bmatrix}, \quad (6)$$

and the Schur complement yields G and G_{obj} with a single run of the solver. It should be noted that although G is obtained in this work using FDTD and FDFD methods, any solution method of choice can be used in principle, including FEM and BEM.

4 Optimization flow

Once precomputation has been performed for a simulation environment, G and G_{obj} may be used for any number of optimization runs with the same environment. Direct Binary Search (DBS) starts with an initial design P_0 , which may be randomly-generated or based on a priori design insight. The inverse of the initial system matrix, $C_0^{-1} = [(I - P_0) + P_0G]^{-1}$, is found and stored, and the objective function is evaluated. At each iteration, a randomly chosen tile in the optimization region is flipped from free space to metal or vice versa. The objective function is evaluated, and if improvement is obtained, the flip is retained and optimization proceeds to the next iteration. Otherwise, another random tile is flipped. Should all possible flips be tested without improvement, the optimization has converged. The DBS process utilizing PNGF is illustrated in Fig. 2(b), and a flowchart is shown in Supplementary Fig. SF1.

At the n th iteration of optimization,

$$\mathbf{x}_{obj,n} = G_{obj}\mathbf{j}_{opt,n} = G_{obj}C_n^{-1}P_n\mathbf{e}_{inc} \quad (7)$$

must be found to evaluate the objective function. Although $C_n^{-1} = [(I - P_n) + P_nG]^{-1}$ could be obtained by solving equation (2) from scratch, since DBS flips only a single tile per iteration, low-rank update methods can be used instead to avoid recomputing the inverse directly, as illustrated in Fig. 2(c) and discussed in the following section.

5 Low-rank update evaluation

After a tile flip, the number M of modified elements in the diagonal design matrix P is the number of field components comprising a tile on the Yee grid. Let $dP_n = P_n - P_{n-1}$ represent the change to P . A wide logical 0–1 projection matrix Q may be constructed such that $dP_n = Q^T H_P Q$, where H_P is a diagonal M -by- M matrix whose entries are the nonzero elements of dP_n . Let $U = Q^T H$ and $V = Q(G - I)$. Then, the update $dC_n = C_n - C_{n-1}$ may be expressed as

$$dC_n = dP_n(G - I) = [Q^T H] [Q(G - I)] = UV. \quad (8)$$

The Woodbury matrix identity [36] may be used to find C_n^{-1} using C_{n-1}^{-1} :

$$C_n^{-1} = (C_{n-1} + UV)^{-1} = C_{n-1}^{-1} - C_{n-1}^{-1}U (I + VC_{n-1}^{-1}U)^{-1} VC_{n-1}^{-1}. \quad (9)$$

However, for many tile flips, the objective function will be worse than that of the previous iteration and C_n^{-1} would be discarded once found. Further performance may be obtained by instead finding $\mathbf{x}_{obj,n}$ directly using C_{n-1}^{-1} . Substituting equation (9)

into $\mathbf{x}_{\text{obj},n} = G_{\text{obj}}C_n^{-1}P_n\mathbf{e}_{\text{inc}}$ yields

$$\mathbf{x}_{\text{obj},n} = G_{\text{obj}} \left[C_{n-1}^{-1} - C_{n-1}^{-1}U (I + VC_{n-1}^{-1}U)^{-1} VC_{n-1}^{-1} \right] P_{n-1}\mathbf{e}_{\text{inc}} \quad (10)$$

Let

$$R_{n-1} = G_{\text{obj}}C_{n-1}^{-1}, \quad (11)$$

$$S_{n-1} = C_{n-1}^{-1}P_{n-1}\mathbf{e}_{\text{inc}}, \quad (12)$$

$$\mathbf{x}_{\text{obj},n-1} = G_{\text{obj}}C_{n-1}^{-1}P_{n-1}\mathbf{e}_{\text{inc}}. \quad (13)$$

Equation (10) becomes

$$\mathbf{x}_{\text{obj},n} = \mathbf{x}_{\text{obj},n-1} - R_{n-1}U (I + VC_{n-1}^{-1}U)^{-1} VS_{n-1}. \quad (14)$$

Since R_{n-1} , S_{n-1} , and $\mathbf{x}_{\text{obj},n-1}$ do not depend on the current design P_n , they may be computed once at the start of a new iteration (after each successful tile flip) and used to rapidly evaluate $\mathbf{x}_{\text{obj},n}$ for new flips until the objective function is improved. Once this occurs, the tile flip is retained, C_n^{-1} of the following iteration is obtained with equation (9), and R_{n-1} and S_{n-1} are updated. It can be shown (Supplementary Note SN.3) that computing $\mathbf{x}_{\text{obj},n}$ for a tile flip and updating C^{-1} for a successful tile flip cost $O(N_{\text{opt}})$ and $O(N_{\text{opt}}^2)$ operations, respectively.

6 Computational efficiency

The cost of objective function evaluation due to flipping a tile is completely independent of the size (N_{sim}) or complexity of the overall simulation domain and grows only linearly with respect to the number of Yee cell components (N_{opt}) inside the optimization region. Thus, for an optimization region of fixed size, the evaluation cost remains unchanged regardless of the surrounding static environment outside the optimization region. If a tile flip improves the objective function, updating the system matrix using equation (9) requires $\mathcal{O}(N_{\text{opt}}^2)$ operations, which is significantly fewer than the $\mathcal{O}(N_{\text{opt}}^3)$ needed to invert C_n directly and also substantially smaller than the $\mathcal{O}(N_{\text{sim}}^3)$ operations required to invert the original full electromagnetic system.

Two examples to illustrate this performance are presented in Fig. 3. First, a planar optimization region of fixed size is considered on the surface of a dielectric substrate, and the evaluation time versus the simulation domain size (N_{sim}) is plotted for PNGF and compared with full-wave electromagnetic solvers as the substrate and simulation dimensions are increased. The second case keeps the simulation (N_{sim}) and substrate size fixed and plots the evaluation time versus the optimization region size (N_{opt}). The simulation environment is a 3D region with a finite dielectric substrate ($\lambda_0 = 10\text{mm}$, $\epsilon_r = 3.5$, thickness: 1.389mm) defined such that its sides are spaced at a fixed distance ($\lambda_0/2$) from Perfectly Matched Layer (PML) absorbing boundary layers [30].

The optimization domain is a square region centered on the substrate, and a ground plane covers the substrate bottom. Tiles ($0.5 \times 0.5\text{mm}$, 3×3 Yee cells) populate the

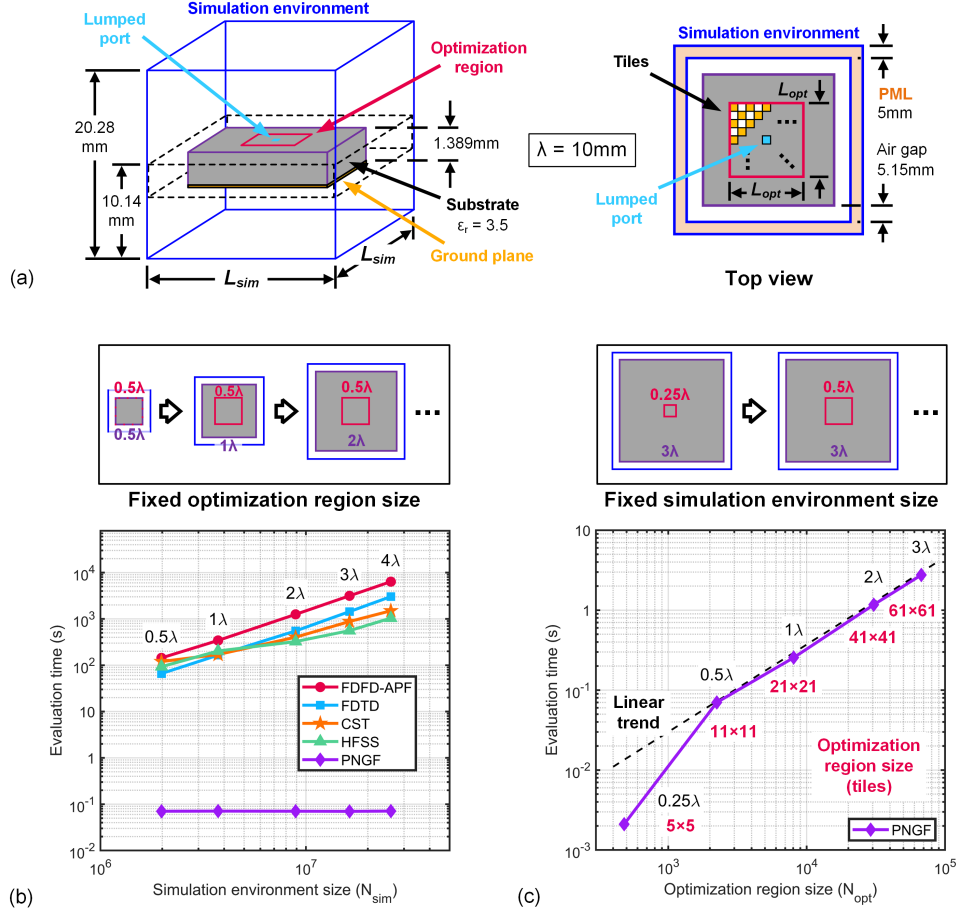


Fig. 3: Runtime performance of the precomputed numerical Green function method during optimization. (a) Simulation environment for benchmarking objective function evaluation using PNGF, where the optimization region is populated with tiles (3×3 voxels each) in a checkerboard pattern; (b) Performance of PNGF compared to full-wave electromagnetic solvers versus simulation environment size with a fixed optimization region, where PNGF is constant-time; (c) Performance of PNGF versus optimization region size for a fixed simulation environment, demonstrating linear runtime with respect to the optimization region size.

optimization region in a checkerboard pattern, a 2D lumped port (3×3 Yee cells) is defined in the center, and the objective function is the reflection coefficient. In comparison to FDFD (using APF as a solver), a custom FDTD solver, HFSS, and CST, PNGF achieves ultra-fast ($< 300\text{ms}$ with optimization regions $< 1\lambda_0$) performance, faster than all other approaches by multiple orders-of-magnitude (940x – $14,600\text{x}$ for the simulation sizes in Fig. 3(b)), while providing an approximation-free solution, in common with the full-wave solvers considered, that is accurate for every possible

optimization region configuration. For any given design, the PNGF results match, to machine precision, those obtained with the solver used for precomputation.

If multiple frequencies are of interest in optimization, a G matrix, with corresponding G_{obj} and C_0^{-1} , may be precomputed for each frequency. The low-rank update evaluation procedure may then be applied to each system. Since each system is independent, finding each \mathbf{x}_{obj} after attempted tile flips and updating each C matrix after successful flips may be performed in parallel without any communication overhead.

Table 1: Comparison of the runtime of direct binary search inverse design using the precomputed numerical Green function method as a solver versus Ansys HFSS and CST Studio.

		Substrate antenna	Switched-beam antenna	Substrate-integrated waveguide
Number of tile flips		652	2478	799
HFSS	Optimization ¹	124h (11.4min × 652)	602h (14.6min × 2478)	173.8h (13.1min × 799)
	Optimization ¹	95h (8.78min × 652)	416h (10.1min × 2478)	192h (14.4min × 799)
CST	Precomputation (FDTD)	27.1min (20.6s × 79)	93.5min (33.2s × 169)	90.0min (41.8s × 129)
	Precomputation (APF)	7.36min	8.89min	11.8min
PNGF	Inverting initial system matrix	4.41s	4.38s	10.94s
	Optimization ²	15.2min (1.40s × 652)	35.7min (0.864s × 2478)	33.7min (2.53s × 799)
	Total (using APF)	22.6min	44.6min	45.7min
	Speedup ³	377x	700x	309x

¹Total optimization times are estimates obtained by extrapolating the runtime of a simulation of the final designs using the number of attempted tile flips in DBS design with PNGF. Coarse mesh settings were used while maintaining reasonable agreement in the reflection coefficient compared to the custom FDTD solver.

²Per-iteration times are averages for each case, computed by dividing the total optimization time by the number of attempted tile flips.

³The speedup figure compares only the optimization time, since precomputation for the PNGF method needs only to be performed once for a given simulation environment, and the precomputed Green function matrices may be reused for any subsequent optimization runs. The smaller of the HFSS and CST times is used for each case.

7 Design studies

For each design study, PNGF is performed with two precomputation approaches: iterative, employing a custom GPU-accelerated FDTD solver, and direct, utilizing

APF. The objective functions and the frequencies at which optimization is performed are detailed in Supplementary Note SN.4. Simulations to verify the final designs are performed with HFSS and the custom FDTD solver. A comparison of the runtime performance is shown in Table 1. The total times for PNGF represent the duration needed to design each device from scratch, with no requisite prior training or pre-existing libraries of simulated designs.

Progress in wireless systems, such as ultrawideband technologies, sub-terahertz/terahertz communications, and Internet of Things, has placed ever-increasing demands on antenna capabilities, performance, and size [37–49]. Planar antennas have been the subject of particular interest [37–41, 44, 47] owing to their ease of fabrication and integration where space is limited. However, traditional topologies, such as patch antennas, are often narrowband or have strongly frequency-dependent radiation patterns. We design a broadband 30GHz center-fed substrate antenna with very wide fractional bandwidth and highly uniform pattern. The substrate antenna design is shown in Fig. 4 with simulated reflection coefficient and radiation patterns. The design exhibits a 10dB return loss bandwidth of 15GHz, corresponding to an exceptional 50% fractional bandwidth. The radiation pattern remains very similar over the entire frequency range, where the gain in the broadside direction is larger than 6.8 dBi with a peak of 8.7dBi at 25GHz.

Advancements in cellular networks have placed ever-growing requirements on antennas for transmitting and receiving multidirectional, ultrawideband signals [39, 40, 42–46]. The multiple-input multiple-output functionality of current cellular technology is typically realized using phased arrays or multiple antenna elements [40, 43–45], whose large electrical size restricts miniaturization. As such, reconfigurable antennas, whose properties may be altered dynamically with inputs (e.g. switches), have garnered substantial attention [46–49]. We design a 30GHz switched-beam antenna for 5G applications, with a switch for selecting between two target beam directions ($\theta = 60^\circ, \phi = 0^\circ$ with switch open; $\theta = -45^\circ, \phi = 0^\circ$ with switch closed). Due to practical equipment limitations, we scaled the inverse-designed antenna up in all dimensions by a factor of 5x before fabrication to shift the center frequency to 6GHz to facilitate measurement. The fabricated SBA is shown in Fig. 5 with the simulated and measured reflection coefficient and radiation patterns versus θ for $\phi = 0$ and $\phi = 45$. The simulations are performed with the fabricated upscaled design, and the measurements agree closely, with a 10dB return loss bandwidth of 0.5GHz and simulated peak gains (with $\phi = 0$) of 8.2dBi (switch open) and 10.6dBi (closed).

Substrate-integrated waveguides (SIWs) comprise a planar substrate enclosed by metal cladding and side walls formed by vias. Owing to their compatibility with printed circuit board fabrication processes, SIWs have attracted considerable interest [50–54]. The fundamental mode is typically excited with a tapered transition from a microstrip feed to the SIW. For compactness, it is desirable to decrease the length of the transition, but this often yields decreased performance. We design a taperless transition from a 50Ω -impedance transmission line to a broadband SIW. The length of the optimization region is more than 4x shorter than the length of a linear taper required to achieve comparable bandwidth, as in [54]. Optimization is performed to minimize the insertion loss over the bandwidth of interest. The fabricated waveguide

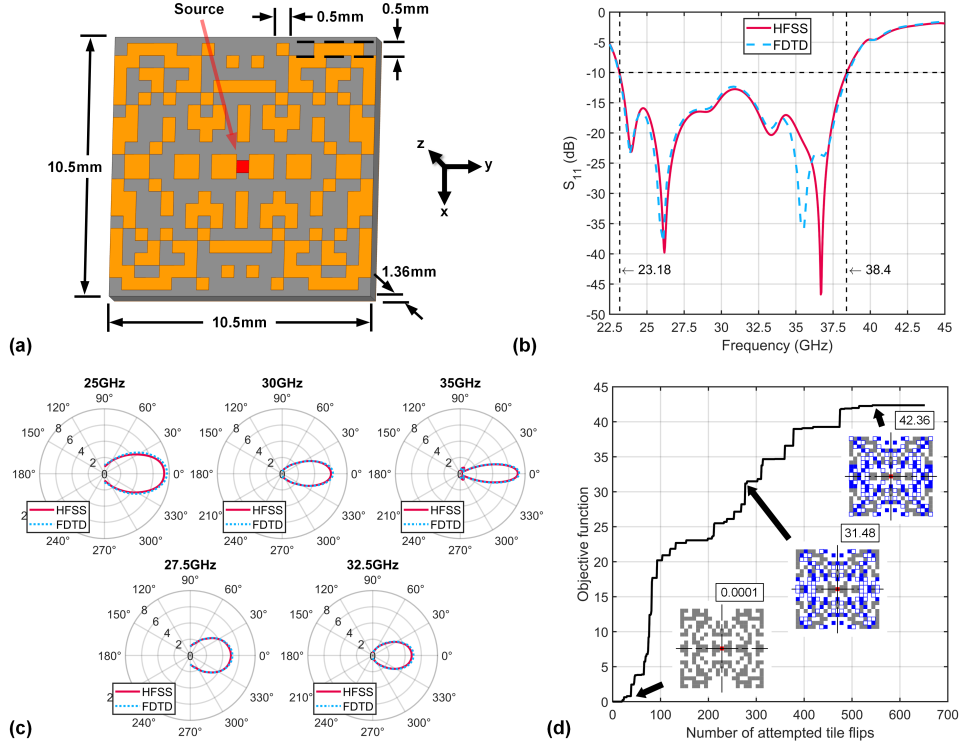


Fig. 4: Broadband 30GHz substrate antenna. (a) Antenna design with indicated dimensions; (b) Simulated S_{11} with HFSS and FDTD solvers; (c) Simulated radiation patterns at frequencies spanning the bandwidth in linear scale relative to an ideal isotropic radiator; (d) Evolution of objective function during inverse design.

section with transitions and the simulated and measured S_{11} and S_{21} are shown in Fig. 6, demonstrating a wide 10dB return-loss bandwidth of approximately 7.7GHz.

8 Conclusions

A new approach for the inverse design of pixelated electromagnetic structures has been presented. By encapsulating the static, unchanging components of the design into a numerical Green function matrix, the method allows any candidate design to be evaluated by solving a linear system with only as many unknowns as the size of the optimization region in the design environment. When utilized with the direct binary search optimization algorithm, a low-rank update technique is employed to accelerate objective function evaluation at each iteration. Runtime improvements up to 700x are obtained versus optimization employing commercial field solvers without compromising the performance of the final design. Future work includes extending the approach to dielectric problems for nanophotonic applications, investigating other optimization algorithms, such as levelset methods and particle swarm optimization,

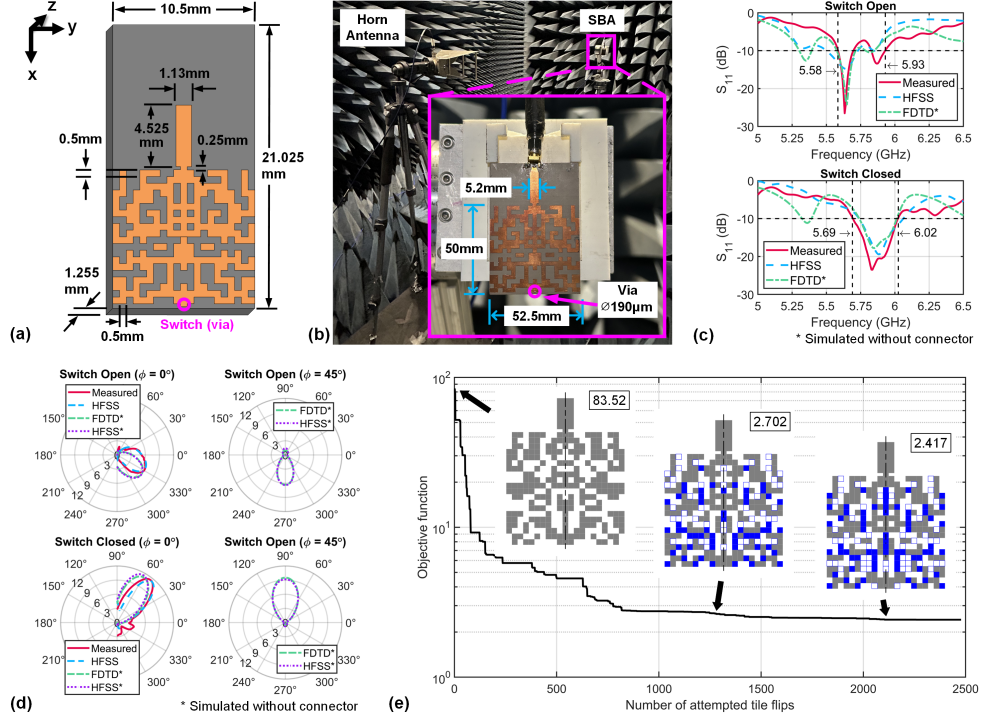


Fig. 5: Reconfigurable switched-beam antenna for 5G cellular applications. (a) 30GHz design with indicated dimensions; (b) Fabricated scaled 6GHz antenna with feed and 2.92mm connector on measurement setup; (c) Simulated and measured S_{11} of 6GHz design with the switch open and closed; (d) Simulated and measured radiation patterns of 6GHz design with the switch open and closed at azimuths of $\phi = 0^\circ$ and $\phi = 45^\circ$, in linear scale relative to an ideal isotropic radiator; (e) Evolution of objective function during inverse design. The measured pattern is normalized to the maximum gain of the simulation results. A slight deviation in the simulated patterns with HFSS and FDTD arises because the connector is not modeled in the FDTD simulation; HFSS simulation without the connector demonstrates excellent agreement with FDTD.

and leveraging alternative solvers to precompute the PNGF matrix, such as boundary integral equation methods and finite element methods. With broad applicability and exceptional performance, the approach is poised to revolutionize the inverse design of electromagnetic devices.

9 Methods

9.1 Finite-difference discretization

For each test case in Fig. 3 and each design study, the same Yee lattice is used for both FDTD and APF precomputations as well as optimization with PNGF. The

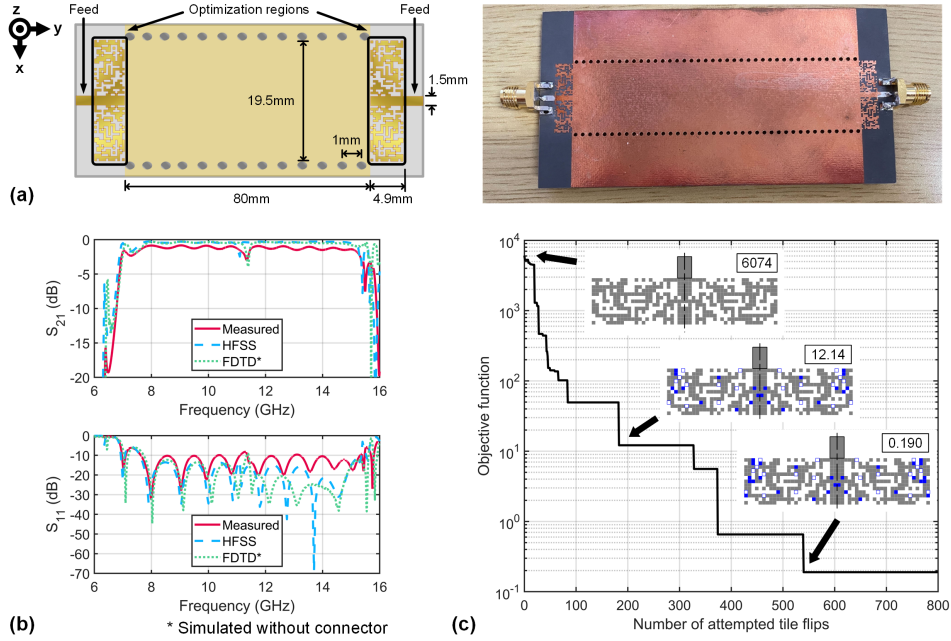


Fig. 6: Broadband 8–15GHz transition from microstrip transmission line to substrate-integrated waveguide. (a) Waveguide section with transitions, microstrip feeds, and 2.92mm connectors on both ends; (b) Simulated and measured S_{11} and S_{21} of the designed structure; (c) Evolution of objective function during inverse design.

optimization regions are rectangular areas made up of faces of adjoining Yee cells. Equivalent polarization current density components, as discussed in Section 3, in x and y are defined on these faces. For example, with tiles comprising 3×3 Yee cells as illustrated in Fig. 1(b), each tile comprises 12 j_x and 12 j_y components, and the number of modified elements M in a tile flip is 24. The current components are co-located with the electric field x and y components on the edges of the Yee cells. Such flat optimization regions are appropriate for modeling the copper-clad utilized in these examples, whose thickness is much smaller than the wavelength. For other applications, however, the optimization region may encompass multiple layers of Yee cells, within which z -components of the current density would also be present. The simulation environment for each design is truncated using PML absorbing boundaries.

9.2 Computational resources

APF is performed with the open-source software MESTI [33]. For large simulation environments, it may be infeasible to use a direct solver owing to the required amount of random access memory, and iterative solvers must be employed, incurring the cost of running N_{opt} field simulations. However, this is not the case for the three design

studies considered in this work, and APF achieves up to 10x decreases in execution time compared to the GPU-accelerated FDTD for precomputation.

For each design study, APF precomputations are run on three 128-core AMD EPYC 7763 nodes, where each precomputation uses 64 cores on one node. These are run in parallel, one for each frequency of optimization in each design. For GPU-accelerated FDTD precomputations, 24 FDTD simulations are run in parallel using the EPYC 7763 nodes with one Nvidia A100-SXM4-80GB GPU per simulation. For optimization, HFSS and CST are run with 128 cores on one node, and the PNGF implementation utilizes the Intel Math Kernel Library (MKL) for linear algebra with the same resources. As optimization is performed at multiple frequencies for each case, evaluation is performed sequentially for each frequency during each iteration.

For the benchmarking of Fig. 3, HFSS and CST are utilized as solvers using the same resources as above, respectively. The FDTD solver is a custom multithreaded implementation using OpenMP and 128 cores on a single node. FDFD is performed with APF as a solver, using 128 cores on a single node.

9.3 Optimization parameters

The substrate antenna design utilizes a 1.3472mm-thick substrate ($\epsilon_r = 3.5$ representing Rogers RO3035) clad with 13.9 μm -thick copper. The bottom copper layer is fully filled as a metal ground reflector, and the optimization region is defined on the top layer. The optimization region comprises a 21x20 grid of tiles, where each tile is 3x3 Yee cells of 0.5 x 0.5mm each. This results in 3786 e_x/j_x and 3780 e_y/j_y components. In view of maximizing the gain in the broadside direction, x and y symmetry are enforced; as such, only 1892 simulations are required when precomputations are performed with FDTD, and 4 tiles are flipped at a time during optimization. A 50 Ω x -directed lumped port in the center is used as the excitation source for field simulations.

The 30GHz SBA design utilizes a 0.508mm-thick Rogers TC350 ($\epsilon_r = 3.5$) clad with 18 μm -thick copper. The bottom layer comprises the ground plane whereas the top design domain is approximately one wavelength square with 21x20 tiles each comprising 3x3 Yee cells of 0.5 x 0.5mm each, giving 3843 e_x/j_x and 3840 e_y/j_y components. With axial symmetry, the number of simulations necessary for precomputations with FDTD is 4053, and 2 tiles are flipped per optimization iteration. The switch is modeled as an ideal metallic via connecting the top and the bottom. The antenna is edge-fed with a microstrip feed; for field simulations, a z -directed 50 Ω lumped port is attached between the feed and the bottom ground. The objective function is set to minimize the return loss and increase the directivity in the directions of interest for each configuration of the switch.

The microstrip-SIW transition design utilizes a 0.508mm-thick Rogers RT/duroid 5880 substrate with $\epsilon_r = 2.2$ with 35 μm -thick copper clad. The bottom layer is completely filled with copper as a ground plane. Each of the two optimization regions, which are constrained to be identical, comprises 52x13 tiles. Since the fundamental mode and the structure are longitudinally symmetric, the optimization region can be reduced in half, to 26 x 13. Each tile comprises 3x3 Yee cells of 0.125mm x 0.125mm

each, corresponding to a total of 6240 e_x/j_x and 6123 e_y/j_y components in the optimization region, and 3091 simulations are required for FDTD precomputations. Given symmetry, 2 tiles are flipped at once during optimization. In field simulations, a z -directed 50Ω lumped port is attached to each microstrip feed end, connecting the ground plane (bottom layer) to the microstrip (top). To design a broadband device, the objective function is set to minimize the insertion loss at five different frequencies. Simulation of the S_{21} of the microstrip-SIW-microstrip structure is accelerated using the technique detailed in Supplementary Note [SN.5](#).

9.4 Device fabrication

The scaled 6GHz SBA is fabricated from a 2.5mm-thick Rogers TC350 substrate with $\epsilon = 3.5$ cladded with 1oz copper. To implement the reconfiguration switch of the fabricated SBA, two antennas are fabricated which differ only in whether the switch via is present (switch closed) or absent (open). A 2.92mm end-launch RF connector (Withwave SM03FS017) is soldered to pads at the end of the microstrip feed of each antenna to provide excitation.

The SIW section is fabricated from the 0.508mm thick RT/duroid 5880 laminate cladded with 1oz copper. Two 2.92mm end-launch RF connectors (Withwave SM03FS007) are soldered at both microstrip feed ends for the S_{11} and S_{21} measurements.

9.5 Measurement system

To measure the reflection coefficient and radiation pattern of the SBA, a measurement setup is established in an anechoic chamber with a vector network analyzer (VNA) (Keysight N5247). For pattern measurements, the SBA is affixed to a two-axis rotary positioner (Diamond Engineering DCP252) driven by stepper motors, and an excitation horn antenna (Com-Power AH-118) is positioned facing the SBA. The pattern is obtained by recording transmission coefficient data with the VNA connected to both antennas, while the elevation and azimuth are swept.

The S_{11} and S_{21} measurements of the microstrip-to-SIW transition are obtained with a VNA (Rohde & Schwarz ZVA-50), with each microstrip connection attached to a VNA port.

Data availability

The data that support the findings of this work are available from the corresponding author upon reasonable request.

Code availability

All code produced during this work are available from the corresponding author at reasonable request.

References

- [1] Johnson, J.M., Rahmat-Samii, V.: Genetic algorithms in engineering electromagnetics. *IEEE Antennas and Propagation Magazine* **39**(4), 7–21 (1997) <https://doi.org/10.1109/74.632992>
- [2] Altshuler, E.E., Linden, D.S.: Wire-antenna designs using genetic algorithms. *IEEE Antennas and Propagation Magazine* **39**(2), 33–43 (1997) <https://doi.org/10.1109/74.584498>
- [3] Robinson, J., Rahmat-Samii, Y.: Particle swarm optimization in electromagnetics. *IEEE Transactions on Antennas and Propagation* **52**(2), 397–407 (2004) <https://doi.org/10.1109/TAP.2004.823969>
- [4] Stadler, S., Igel, J.: Developing Realistic FDTD GPR Antenna Surrogates by Means of Particle Swarm Optimization. *IEEE Transactions on Antennas and Propagation* **70**(6), 4259–4272 (2022) <https://doi.org/10.1109/TAP.2022.3142335>
- [5] Jin, N., Rahmat-Samii, Y.: Advances in Particle Swarm Optimization for Antenna Designs: Real-Number, Binary, Single-Objective and Multiobjective Implementations. *IEEE Transactions on Antennas and Propagation* **55**(3), 556–567 (2007) <https://doi.org/10.1109/TAP.2007.891552>
- [6] Lalau-Keraly, C.M., Bhargava, S., Miller, O.D., Yablonovitch, E.: Adjoint shape optimization applied to electromagnetic design. *Optics Express* **21**(18), 21693–21701 (2013) <https://doi.org/10.1364/OE.21.021693>
- [7] Zhu, R., Qiu, T., Wang, J., Sui, S., Hao, C., Liu, T., Li, Y., Feng, M., Zhang, A., Qiu, C.-W., Qu, S.: Phase-to-pattern inverse design paradigm for fast realization of functional metasurfaces via transfer learning. *Nature Communications* **12**(1), 2974 (2021) <https://doi.org/10.1038/s41467-021-23087-y>
- [8] Naseri, P., Hum, S.V.: A Generative Machine Learning-Based Approach for Inverse Design of Multilayer Metasurfaces. *IEEE Transactions on Antennas and Propagation* **69**(9), 5725–5739 (2021) <https://doi.org/10.1109/TAP.2021.3060142>
- [9] Hou, J., Lin, H., Xu, W., Tian, Y., Wang, Y., Shi, X., Deng, F., Chen, L.: Customized Inverse Design of Metamaterial Absorber Based on Target-Driven Deep Learning Method. *IEEE Access* **8**, 211849–211859 (2020) <https://doi.org/10.1109/ACCESS.2020.3038933>
- [10] Mohammadi Estakhri, N., Edwards, B., Engheta, N.: Inverse-designed metastructures that solve equations. *Science* **363**(6433), 1333–1338 (2019) <https://doi.org/10.1126/science.aaw2498>

- [11] Karahan, E.A., Liu, Z., Gupta, A., Shao, Z., Zhou, J., Khankhoje, U., Sengupta, K.: Deep-learning enabled generalized inverse design of multi-port radio-frequency and sub-terahertz passives and integrated circuits. *Nature Communications* **15**(1), 10734 (2024) <https://doi.org/10.1038/s41467-024-54178-1>
- [12] Karahan, E.A., Liu, Z., Sengupta, K.: Deep-Learning-Based Inverse-Designed Millimeter-Wave Passives and Power Amplifiers. *IEEE Journal of Solid-State Circuits* **58**(11), 3074–3088 (2023) <https://doi.org/10.1109/JSSC.2023.3276315>
- [13] Yang, X., Zhao, Y., Wan, M., Chen, Y., Zhou, H., Nie, Z., Yang, D.: Circularly Polarized Antenna Array Synthesis Based on Machine-Learning-Assisted Surrogate Modeling. *IEEE Transactions on Antennas and Propagation* **72**(2), 1469–1482 (2024) <https://doi.org/10.1109/TAP.2023.3335808>
- [14] Molesky, S., Lin, Z., Piggott, A.Y., Jin, W., Vucković, J., Rodriguez, A.W.: Inverse design in nanophotonics. *Nature Photonics* **12**(11), 659–670 (2018) <https://doi.org/10.1038/s41566-018-0246-9>
- [15] Li, Z., Pestourie, R., Park, J.-S., Huang, Y.-W., Johnson, S.G., Capasso, F.: Inverse design enables large-scale high-performance meta-optics reshaping virtual reality. *Nature Communications* **13**(1), 2409 (2022) <https://doi.org/10.1038/s41467-022-29973-3>
- [16] Hughes, T.W., Minkov, M., Williamson, I.A.D., Fan, S.: Adjoint Method and Inverse Design for Nonlinear Nanophotonic Devices. *ACS Photonics* **5**(12), 4781–4787 (2018) <https://doi.org/10.1021/acsp Photonics.8b01522>
- [17] Peurifoy, J., Shen, Y., Jing, L., Yang, Y., Cano-Renteria, F., DeLacy, B.G., Joannopoulos, J.D., Tegmark, M., Soljačić, M.: Nanophotonic particle simulation and inverse design using artificial neural networks. *Science Advances* **4**(6), 4206 (2018) <https://doi.org/10.1126/sciadv.aar4206>
- [18] Roberts, G., Ballew, C., Zheng, T., Garcia, J.C., Camayd-Muñoz, S., Hon, P.W.C., Faraon, A.: 3D-patterned inverse-designed mid-infrared metaoptics. *Nature Communications* **14**(1), 2768 (2023) <https://doi.org/10.1038/s41467-023-38258-2>
- [19] Ma, W., Liu, Z., Kudyshev, Z.A., Boltasseva, A., Cai, W., Liu, Y.: Deep learning for the design of photonic structures. *Nature Photonics* **15**(2), 77–90 (2021) <https://doi.org/10.1038/s41566-020-0685-y>
- [20] Camacho, M., Edwards, B., Engheta, N.: A single inverse-designed photonic structure that performs parallel computing. *Nature Communications* **12**(1), 1466 (2021) <https://doi.org/10.1038/s41467-021-21664-9>
- [21] Piggott, A.Y., Lu, J., Lagoudakis, K.G., Petykiewicz, J., Babinec, T.M., Vučković,

- J.: Inverse design and demonstration of a compact and broadband on-chip wavelength demultiplexer. *Nature Photonics* **9**(6), 374–377 (2015) <https://doi.org/10.1038/nphoton.2015.69>
- [22] Wiecha, P.R., Muskens, O.L.: Deep Learning Meets Nanophotonics: A Generalized Accurate Predictor for Near Fields and Far Fields of Arbitrary 3D Nanostructures. *Nano Letters* **20**(1), 329–338 (2020) <https://doi.org/10.1021/acs.nanolett.9b03971>
- [23] Sanchez-Lengeling, B., Aspuru-Guzik, A.: Inverse molecular design using machine learning: Generative models for matter engineering. *Science* **361**(6400), 360–365 (2018) <https://doi.org/10.1126/science.aat2663>
- [24] Kumar, S., Tan, S., Zheng, L., Kochmann, D.M.: Inverse-designed spinodoid metamaterials. *npj Computational Materials* **6**(1), 1–10 (2020) <https://doi.org/10.1038/s41524-020-0341-6>
- [25] Ha, C.S., Yao, D., Xu, Z., Liu, C., Liu, H., Elkins, D., Kile, M., Deshpande, V., Kong, Z., Bauchy, M., Zheng, X.R.: Rapid inverse design of metamaterials based on prescribed mechanical behavior through machine learning. *Nature Communications* **14**(1), 5765 (2023) <https://doi.org/10.1038/s41467-023-40854-1>
- [26] Coli, G.M., Boattini, E., Filion, L., Dijkstra, M.: Inverse design of soft materials via a deep learning-based evolutionary strategy. *Science Advances* **8**(3), 6731 (2022) <https://doi.org/10.1126/sciadv.abj6731>
- [27] Zunger, A.: Inverse design in search of materials with target functionalities. *Nature Reviews Chemistry* **2**(4), 1–16 (2018) <https://doi.org/10.1038/s41570-018-0121>
- [28] Kennedy, J., Eberhart, R.: Particle swarm optimization. In: Proceedings of ICNN'95 - International Conference on Neural Networks, vol. 4, pp. 1942–19484 (1995). <https://doi.org/10.1109/ICNN.1995.488968>
- [29] Alizadeh, R., Allen, J.K., Mistree, F.: Managing computational complexity using surrogate models: a critical review. *Research in Engineering Design* **31**(3), 275–298 (2020) <https://doi.org/10.1007/s00163-020-00336-7>
- [30] Taflove, A., Hagness, S.C.: *Computational Electrodynamics: The Finite-difference Time-domain Method*, 3rd edn. Artech House, Norwood (2005)
- [31] Markkanen, J., Yla-Oijala, P., Sihvola, A.: Discretization of Volume Integral Equation Formulations for Extremely Anisotropic Materials. *IEEE Transactions on Antennas and Propagation* **60**(11), 5195–5202 (2012) <https://doi.org/10.1109/TAP.2012.2207675>

- [32] Harrington, R.F.: The Method of Moments in Electromagnetics. *Journal of Electromagnetic Waves and Applications* **1**(3), 181–200 (1987) <https://doi.org/10.1163/156939387X00018>
- [33] Lin, H.-C., Wang, Z., Hsu, C.W.: Fast multi-source nanophotonic simulations using augmented partial factorization. *Nature Computational Science* **2**(12), 815–822 (2022) <https://doi.org/10.1038/s43588-022-00370-6>
- [34] Zhang, F. (ed.): *The Schur Complement and Its Applications. Numerical Methods and Algorithms*, vol. 4. Springer, New York (2005)
- [35] Ansys Canada Ltd.: Understanding the mode overlap calculation (2024). <https://optics.ansys.com/hc/en-us/articles/360034396834-Understanding-the-mode-overlap-calculation>
- [36] Bayin, S.: *Mathematical Methods in Science and Engineering*. Wiley, Hoboken, New Jersey (2006)
- [37] Kimionis, J., Georgiadis, A., Daskalakis, S.N., Tentzeris, M.M.: A printed millimetre-wave modulator and antenna array for backscatter communications at gigabit data rates. *Nature Electronics* **4**(6), 439–446 (2021) <https://doi.org/10.1038/s41928-021-00588-8>
- [38] Wu, G.-B., Dai, J.Y., Shum, K.M., Chan, K.F., Cheng, Q., Cui, T.J., Chan, C.H.: A universal metasurface antenna to manipulate all fundamental characteristics of electromagnetic waves. *Nature Communications* **14**(1), 5155 (2023) <https://doi.org/10.1038/s41467-023-40717-9>
- [39] Zhao, W., Ni, H., Ding, C., Liu, L., Fu, Q., Lin, F., Tian, F., Yang, P., Liu, S., He, W., Wang, X., Huang, W., Zhao, Q.: 2D Titanium carbide printed flexible ultrawideband monopole antenna for wireless communications. *Nature Communications* **14**(1), 278 (2023) <https://doi.org/10.1038/s41467-022-35371-6>
- [40] Ahmad, A., Choi, D.-y., Ullah, S.: A compact two elements MIMO antenna for 5G communication. *Scientific Reports* **12**(1), 3608 (2022) <https://doi.org/10.1038/s41598-022-07579-5>
- [41] Zheng, Y., Sideris, C.: Ultra-fast Simulation and Inverse Design of Metallic Antennas. In: *2023 IEEE/MTT-S International Microwave Symposium - IMS 2023*, pp. 351–354 (2023). <https://doi.org/10.1109/IMS37964.2023.10187915>
- [42] Islam, S., Zada, M., Yoo, H.: Highly Compact Integrated Sub-6 GHz and Millimeter-Wave Band Antenna Array for 5G Smartphone Communications. *IEEE Transactions on Antennas and Propagation* **70**(12), 11629–11638 (2022) <https://doi.org/10.1109/TAP.2022.3209310>
- [43] Liu, L., Cheung, S.W., Yuk, T.I.: Compact MIMO Antenna for Portable Devices

- in UWB Applications. *IEEE Transactions on Antennas and Propagation* **61**(8), 4257–4264 (2013) <https://doi.org/10.1109/TAP.2013.2263277>
- [44] Liu, W.E.I., Chen, Z.N., Qing, X., Shi, J., Lin, F.H.: Miniaturized Wideband Metasurface Antennas. *IEEE Transactions on Antennas and Propagation* **65**(12), 7345–7349 (2017) <https://doi.org/10.1109/TAP.2017.2761550> .
- [45] Kibaroglu, K., Sayginer, M., Phelps, T., Rebeiz, G.M.: A 64-Element 28-GHz Phased-Array Transceiver With 52-dBm EIRP and 8–12-Gb/s 5G Link at 300 Meters Without Any Calibration. *IEEE Transactions on Microwave Theory and Techniques* **66**(12), 5796–5811 (2018) <https://doi.org/10.1109/TMTT.2018.2854174>
- [46] Dadgarpour, A., Zarghooni, B., Virdee, B.S., Denidni, T.A.: One- and Two-Dimensional Beam-Switching Antenna for Millimeter-Wave MIMO Applications. *IEEE Transactions on Antennas and Propagation* **64**(2), 564–573 (2016) <https://doi.org/10.1109/TAP.2015.2508478>
- [47] Karmokar, D.K., Esselle, K.P., Hay, S.G.: Fixed-Frequency Beam Steering of Microstrip Leaky-Wave Antennas Using Binary Switches. *IEEE Transactions on Antennas and Propagation* **64**(6), 2146–2154 (2016) <https://doi.org/10.1109/TAP.2016.2546949>
- [48] Yang, G.-W., Li, J., Cao, B., Wei, D., Zhou, S.-G., Deng, J.: A Compact Reconfigurable Microstrip Antenna With Multidirectional Beam and Multipolarization. *IEEE Transactions on Antennas and Propagation* **67**(2), 1358–1363 (2019) <https://doi.org/10.1109/TAP.2018.2883663>
- [49] Mackertich-Sengerdy, G., Campbell, S.D., Werner, D.H.: Tailored compliant mechanisms for reconfigurable electromagnetic devices. *Nature Communications* **14**(1), 683 (2023) <https://doi.org/10.1038/s41467-023-36143-6>
- [50] Uchimura, H., Takenoshita, T., Fujii, M.: Development of a "laminated waveguide". *IEEE Transactions on Microwave Theory and Techniques* **46**(12), 2438–2443 (1998) <https://doi.org/10.1109/22.739232>
- [51] Deslandes, D., Wu, K.: Accurate modeling, wave mechanisms, and design considerations of a substrate integrated waveguide. *IEEE Transactions on Microwave Theory and Techniques* **54**(6), 2516–2526 (2006) <https://doi.org/10.1109/TMTT.2006.875807>
- [52] Deslandes, D., Wu, K.: Integrated microstrip and rectangular waveguide in planar form. *IEEE Microwave and Wireless Components Letters* **11**(2), 68–70 (2001) <https://doi.org/10.1109/7260.914305>
- [53] Lee, J.-H., Kidera, N., DeJean, G., Pinel, S., Laskar, J., Tentzeris, M.M.: A V-band front-end with 3-D integrated cavity filters/duplexers and antenna in LTCC

technologies. IEEE Transactions on Microwave Theory and Techniques **54**(7), 2925–2936 (2006) <https://doi.org/10.1109/TMTT.2006.877440>

- [54] Elsayaf, M.H.A., Sideris, C.: Concurrent Multi-Mode Excitation for Mode Division Multiplexing over Substrate Integrated Waveguides. In: 2023 IEEE/MTT-S International Microwave Symposium - IMS 2023, pp. 505–508 (2023). <https://doi.org/10.1109/IMS37964.2023.10188009>

Acknowledgements

The authors gratefully acknowledge support by the Air Force Office of Scientific Research (FA9550-20-1-0087 and FA9550-25-1-0020) and the National Science Foundation (CCF-2047433).

Ethics declarations

Competing interests

The authors declare no competing interests.

Supplementary Information

Contents

Supplementary Notes	1
SN.1 Current equivalence derivation	1
SN.2 Finite-difference formulation for augmented partial factorization	2
SN.3 Cost of system matrix update and objective function evaluation	3
SN.4 Objective functions for design studies	4
SN.5 Accelerated computation of waveguide transition scattering parameters	4
Supplementary Figure 1	8
Supplementary Figure 2	8

Supplementary Notes

SN.1 Current equivalence derivation

The electric field-only Maxwell's equations are

$$\omega^2 \epsilon \mathbf{E} - \nabla \times \mu^{-1} \nabla \times \mathbf{E} = i\omega \mathbf{J} \quad (\text{S1})$$

Assuming no magnetic materials (these can be incorporated with additional magnetic polarization densities but are not relevant to the problems considered in this work), $\mu = \mu_0$. We can introduce an equivalent polarization density $\mathbf{J}_p(\mathbf{r}) = i\omega \epsilon_0 (\epsilon_r(\mathbf{r}) - 1) \mathbf{E}(\mathbf{r})$ to express the total electric fields \mathbf{E} in the presence of an inhomogeneous dielectric volume $\epsilon_r(\mathbf{r})$ and rewrite in terms of the free-space Maxwell's equations:

$$\omega^2 \epsilon \mu_0 \mathbf{E} - \nabla \times \nabla \times \mathbf{E} = i\omega \mu_0 \mathbf{J}_p \quad (\text{S2})$$

We seek to find \mathbf{J}_p to produce the same \mathbf{E} in response to an incident excitation field \mathbf{E}_{inc} in free space, as produced by the dielectric material(s) and metallic tile(s) for a candidate design. In free space, the total electric field due to the field produced by a volume electric current density \mathbf{J} and incident field \mathbf{E}_{inc} is given by

$$\mathbf{E} = \mathbf{E}_{\text{inc}} - \int_V \overline{\overline{G_0}}(\mathbf{r}, \mathbf{r}') \mathbf{J}(\mathbf{r}') dV' \quad (\text{S3})$$

where $\overline{\overline{G}}_0(\mathbf{r}, \mathbf{r}')$ is the free-space Green's tensor. Substituting in $\mathbf{J}_\mathbf{p}$ and multiplying both sides of the equation by $i\omega\epsilon_0(\epsilon_r(\mathbf{r}) - 1)$ yields

$$i\omega\epsilon_0(\epsilon_r(\mathbf{r}) - 1)\mathbf{E} = i\omega\epsilon_0(\epsilon_r(\mathbf{r}) - 1)\mathbf{E}_{inc} - i\omega\epsilon_0(\epsilon_r(\mathbf{r}) - 1) \int_V \overline{\overline{G}}_0(\mathbf{r}, \mathbf{r}')\mathbf{J}_\mathbf{p} dV' \quad (\text{S4})$$

By using $\mathbf{J}_\mathbf{p}(\mathbf{r}) = i\omega\epsilon_0(\epsilon_r(\mathbf{r}) - 1)\mathbf{E}(\mathbf{r})$, this can be rewritten as:

$$\mathbf{J}_\mathbf{p}(\mathbf{r}) = i\omega\epsilon_0(\epsilon_r(\mathbf{r}) - 1)\mathbf{E}_{inc} - i\omega\epsilon_0(\epsilon_r(\mathbf{r}) - 1) \int_V \overline{\overline{G}}_0(\mathbf{r}, \mathbf{r}')\mathbf{J}_\mathbf{p} dV' \quad (\text{S5})$$

The permittivity $\epsilon_r(\mathbf{r})$ for a metal may be represented as $\epsilon_r(\mathbf{r}) = 1 + \frac{\sigma(\mathbf{r})}{i\omega\epsilon_0}$, where $\sigma(\mathbf{r})$ is the material conductivity. Thus,

$$\mathbf{J}_\mathbf{p}(\mathbf{r}) = \sigma(\mathbf{r})\mathbf{E}_{inc} - \sigma(\mathbf{r}) \int_V \overline{\overline{G}}_0(\mathbf{r}, \mathbf{r}')\mathbf{J}_\mathbf{p} dV' \quad (\text{S6})$$

Throughout the optimization region, σ is either 0 (free space) or ∞ (metal, represented by perfect electrical conductor). As such, by introducing the auxiliary quantity $p(\mathbf{r}) = \frac{\sigma(\mathbf{r})}{1+\sigma(\mathbf{r})}$ and therefore $\sigma(\mathbf{r}) = \frac{p(\mathbf{r})}{1-p(\mathbf{r})}$ equation (1) in the main text is obtained and reproduced here:

$$p(\mathbf{r})\mathbf{E}_{inc} = (1 - p(\mathbf{r}))\mathbf{J}_\mathbf{p}(\mathbf{r}) + p(\mathbf{r}) \int_V \overline{\overline{G}}_0(\mathbf{r}, \mathbf{r}')\mathbf{J}_\mathbf{p} dV' \quad (\text{S7})$$

Note that the variable $p(\mathbf{r})$ was introduced such that $p = 0$ corresponds to $\sigma = 0$ (free-space) and $p = 1$ corresponds to $\sigma = \infty$ (PEC) so that the resulting numerical system can express both free-space and PEC with finite quantities. This resulting integral equation can be discretized using a suitable method of choice as discussed in the main text, and the Green's tensor $\overline{\overline{G}}_0$ may be replaced with a numerically computed Green function to incorporate any background environment (arbitrary materials, metals, etc.) into the simulation domain.

SN.2 Finite-difference formulation for augmented partial factorization

The FDFD linear system, which is a frequency-domain discretization of Maxwell's equations, is given by

$$D^E \mathbf{E} = -i\omega \text{diag}(\mu) \mathbf{H} \quad (\text{S8})$$

$$D^H \mathbf{H} = i\omega \text{diag}(\epsilon) \mathbf{E} + \mathbf{J} \quad (\text{S9})$$

where D^E and D^H are matrices that discretize the curl operator using central finite differences, \mathbf{E} is the electric field, \mathbf{J} is the current density, ω is the frequency, and i is

the imaginary unit. The magnetic field \mathbf{H} may be eliminated, yielding

$$[\omega^2 \text{diag}(\epsilon) - D^H \text{diag}(\mu^{-1}) D^E] \mathbf{E} = i\omega \mathbf{J} \quad (\text{S10})$$

The matrix $1/(i\omega) \cdot [\omega^2 \text{diag}(\epsilon) - D^H \text{diag}(\mu^{-1}) D^E]$ is the FDFD system matrix A , and solving the linear system $A\mathbf{E} = \mathbf{J}$ by inverting A yields the electric fields produced due to time-harmonic sources represented by \mathbf{J} .

The matrix $B^T A^{-1} B$ in equation (3), which is the G matrix considered in precomputation, corresponds to

$$B^T A^{-1} B = B^T i\omega [\omega^2 \text{diag}(\epsilon) - D^H \text{diag}(\mu^{-1}) D^E] B \quad (\text{S11})$$

and may be computed with a sparse direct solver such as APF, as discussed in Section 3. Multiple A matrices may be set up for each frequency ω of interest and used with APF to obtain G matrices for each ω .

SN.3 Cost of system matrix update and objective function evaluation

For updates to the PNGF system matrix C using equation (9), the matrix multiplication $VC_{n-1}^{-1}U$ may take up to the order of M^3 operations to perform. Carrying out the matrix inversion for $(VC_{n-1}^{-1}U)^{-1}$ requires in general $\mathcal{O}(M^3)$ operations. The product

$$C_{n-1}^{-1}U (I + VC_{n-1}^{-1}U)^{-1} VC_{n-1}^{-1} \quad (\text{S12})$$

is a multiplication of matrices with sizes of, from left to right, $N_{opt} \times N_{opt}$, $N_{opt} \times M$, $M \times M$, $M \times N_{opt}$, and $N_{opt} \times N_{opt}$. When performed in the appropriate order, the number of operations involved is $3MN_{opt}^2 + M^2N_{opt}$. Since $M \ll N_{opt}$, the first term dominates the required number of operations for the multiplication, including the inversion of $I + VC_{n-1}^{-1}U$. Therefore, the overall cost of updating the system matrix is $\mathcal{O}(MN_{opt}^2)$.

For evaluating the objective function using equation (14), the product

$$R_{n-1}U (I + VC_{n-1}^{-1}U)^{-1} VS_{n-1} \quad (\text{S13})$$

is a multiplication of matrices of sizes of, from left to right, $N_{obj} \times N_{opt}$, $N_{opt} \times M$, $M \times M$, $M \times N_{opt}$, and $N_{opt} \times 1$. The quantity $S_{n-1} = C_{n-1}^{-1}P_{n-1}\mathbf{e}_{\text{inc}}$ has a single column since \mathbf{e}_{inc} is a vector. Evaluating the product (S13) from right to left requires $(N_{obj} + 2M)N_{opt} + M^2$ operations. Like with updating the system matrix, since $M \ll N_{opt}$, the first term is dominant compared to the matrix multiplication and inversion. Thus, the cost of evaluating the objective function is $\mathcal{O}((N_{obj} + 2M)N_{opt})$.

SN.4 Objective functions for design studies

SN.4.1 Substrate antenna

The objective function is specified at five frequencies {25, 27.5, 30, 32.5, 35GHz} with the goal of maximizing

$$f_n = \frac{|S_{11,n}|}{1 + e^{(3-D_n(0,0))}} + \frac{5D_n(0,0)}{1 + e^{(10-|S_{11,n}|)}}, \quad (\text{S14})$$

where each frequency is indexed as n , $S_{11,n}$ is the reflection coefficient, and $D_n(\theta, \phi)$ is the directivity. The coefficients are empirical and are found for the best optimization results. The harmonic mean is used to aggregate the objective functions at each frequency:

$$f_{obj} = \frac{1}{\frac{1}{f_1} + \frac{1}{f_2} + \frac{1}{f_3} + \frac{1}{f_4} + \frac{1}{f_5}} \quad (\text{S15})$$

SN.4.2 Switched-beam antenna

The objective function is found at three frequencies {29.5, 30, 30.5GHz} with the aim of minimizing

$$\begin{aligned} f_n = & 3.0 \cdot 3.3 \cdot \left(|S_{11,n}^{on}| + |S_{11,n}^{off}| \right) \\ & + 8.0 \cdot \left(\frac{1}{D_n^{on}(45^\circ, 270^\circ)} + \frac{1}{D_n^{off}(45^\circ, 90^\circ)} \right) \\ & + 1.0 \cdot \left(D_n^{on}(45^\circ, 90^\circ) + D_n^{off}(45^\circ, 270^\circ) \right), \end{aligned} \quad (\text{S16})$$

where each frequency is indexed as n , $S_{11,n}^{on}$ and $S_{11,n}^{off}$ are the reflection coefficients with the switch closed and open, respectively, and $D_n^{on}(\theta, \phi)$ and $D_n^{off}(\theta, \phi)$ are the directivities in each case. As with the substrate antenna, the coefficients are found empirically and the harmonic mean is used.

SN.4.3 Substrate-integrated waveguide

The objective function is defined at five frequencies {11, 11.5, 12, 12.5, 13GHz}, with the target of minimizing

$$f_n = (1 - |S_{21,n}|)^2 \quad (\text{S17})$$

where $S_{21,n}$ is the transmission coefficient at frequency n and, as before, the harmonic mean is employed.

SN.5 Accelerated computation of waveguide transition scattering parameters

Traditionally, the S_{21} of a two-port device is performed by simulating the entire structure with two lumped ports, an input port and an output port. For the microstrip-SIW transition design study, however, the microstrip-SIW-microstrip structure may

be subdivided into three segments as illustrated in Supplementary Fig. SF2(a): first; propagation from the input (port 1) through the first transition (microstrip-SIW) to the SIW; second, propagation through the SIW itself; and third, propagation from the SIW to the second transition (SIW-microstrip) to the output (port 2). These segments are indexed A, B, and C, respectively. This allows acceleration of finding the S_{21} since segment B does not require full-wave simulation. The two lumped ports on the outer interface of segments A and C are retained, and we add wave ports to the inner interface of these segments, over the waveguide cross-section, for excitation at the fundamental mode. Since segments A and C are identical, only one such microstrip-SIW transition segment needs to be simulated, and the S_{21} may be obtained utilizing propagation matrices of the SIW fundamental mode.

The full two-port structure may be described using the following impedance matrix

$$\begin{bmatrix} V_1 \\ V_2 \end{bmatrix} = \begin{bmatrix} Z_{11} & Z_{12} \\ Z_{21} & Z_{22} \end{bmatrix} \begin{bmatrix} I_1 \\ I_2 \end{bmatrix} \quad (\text{S18})$$

where V_1 and V_2 are the voltages at each port and I_1 and I_2 are the currents flowing into the structure from each port. For each segment of the structure, the corresponding mixed two-port network can be represented by mixed parameter matrices as follows:

$$\begin{bmatrix} V_1 \\ \beta_{A2} \end{bmatrix} = \begin{bmatrix} A_{11} & A_{12} \\ A_{21} & A_{22} \end{bmatrix} \begin{bmatrix} I_1 \\ \alpha_{A2} \end{bmatrix} \quad (\text{S19})$$

$$\begin{bmatrix} \beta_{B1} \\ \beta_{B2} \end{bmatrix} = \begin{bmatrix} B_{11} & B_{12} \\ B_{21} & B_{22} \end{bmatrix} \begin{bmatrix} \alpha_{B1} \\ \alpha_{B2} \end{bmatrix} \quad (\text{S20})$$

$$\begin{bmatrix} \beta_{C1} \\ V_2 \end{bmatrix} = \begin{bmatrix} C_{11} & C_{12} \\ C_{21} & C_{22} \end{bmatrix} \begin{bmatrix} \alpha_{C1} \\ I_2 \end{bmatrix} \quad (\text{S21})$$

where A links V_1 and I_1 of the lumped port of segment A to the complex transmission coefficients α of the forward-propagating wave and β of the backward-propagating wave of the wave port at the SIW interface, B links the transmission coefficients of the ends of segment B, and C links the transmission coefficients of the wave port to V_2 and I_2 of the lumped port of segment C. The transmission coefficients α and β may be found with

$$\alpha_m = \frac{1}{4} \left(\frac{\int \mathbf{E}_{\text{in}} \times \mathbf{H}_{\text{m}}^* d\mathbf{S}}{N_m} + \frac{\int \mathbf{E}_{\text{m}}^* \times \mathbf{H}_{\text{in}} d\mathbf{S}}{N_m^*} \right) \quad (\text{S22})$$

$$\beta_m = \frac{1}{4} \left(\frac{\int \mathbf{E}_{\text{in}} \times \mathbf{H}_{\text{m}}^* d\mathbf{S}}{N_m} - \frac{\int \mathbf{E}_{\text{m}}^* \times \mathbf{H}_{\text{in}} d\mathbf{S}}{N_m^*} \right), \quad (\text{S23})$$

where

$$N_m = \frac{1}{2} \int \mathbf{E}_{\text{m}} \times \mathbf{H}_{\text{m}}^* d\mathbf{S}. \quad (\text{S24})$$

The quantities \mathbf{E}_{m} and \mathbf{H}_{m} are the field values of the m th mode of the waveguide cross-section, which may be computed with a mode solver. In this case, the fundamental mode ($m = 1$) is of interest. The quantities \mathbf{E}_{in} and \mathbf{H}_{in} are the field values over the

waveguide cross-section as excited by a port. N_m is a complex value whose real part is the power of mode m .

The coupling conditions between the three sections are given by $\beta_{A2} = \alpha_{B1}$, $\beta_{B2} = \alpha_{C1}$, $\beta_{C1} = \alpha_{B2}$, and $\beta_{B1} = \alpha_{A2}$. Moreover, based on the wave propagation principle in a uniform section of waveguide, there will be no attenuation when it is excited by a proper mode excitation at a frequency above the waveguide cutoff frequency, which yields $B_{11} = B_{22} = 0$. Furthermore, since segments A and C are identical but mirrored,

$$\begin{cases} C_{11} = A_{22} \\ C_{12} = A_{21} \\ C_{21} = A_{12} \\ C_{22} = A_{11} \end{cases} \quad (\text{S25})$$

With these conditions, equations (S19-S21) may be combined into equation (S18), where

$$Z_{11} = Z_{22} = \frac{A_{11} + B_{12}B_{21}A_{12}A_{21}A_{22} - B_{12}B_{21}A_{11}A_{12}A_{22}}{1 - B_{21}A_{22}^2B_{12}} \quad (\text{S26})$$

$$Z_{12} = Z_{21} = \frac{B_{12}A_{12}A_{21} + B_{12}A_{11}A_{22} - B_{12}A_{11}A_{12}}{1 - B_{21}A_{22}^2B_{12}} \quad (\text{S27})$$

It is known that the waveguide modes, which are B_{12} and B_{21} in this case, have analytical solutions given by $e^{-j\beta z}$, where β is the propagation constant for the fundamental mode and z is the length of segment B. As such, only the A matrix parameters need to be found with simulation. Two simulations are necessary: one where a current source on the lumped port is used as excitation, to find

$$A_{11} = \frac{V_{A1}}{I_{A1}} \Big|_{\alpha_{A2}=0} \quad (\text{S28})$$

$$A_{21} = \frac{\beta_{A2}}{I_{A1}} \Big|_{\alpha_{A2}=0} \quad (\text{S29})$$

and another where excitation of the fundamental mode is provided by the wave port, to find

$$A_{12} = \frac{V_{A1}}{\alpha_{A2}} \Big|_{I_{A1}=0} \quad (\text{S30})$$

$$A_{22} = \frac{\beta_{A2}}{\alpha_{A2}} \Big|_{I_{A1}=0}. \quad (\text{S31})$$

This is depicted in Supplementary Fig. SF2(b). To find these parameters, the E fields on the lumped port and the E and H fields over the cross-section of the wave port are recorded for both simulations. Once the Z matrix is obtained, S-parameters may be

computed by conversion from Z-parameters. For example,

$$S_{21} = \frac{2Z_{21}Z_0}{(Z_{11} + Z_0)(Z_{22} + Z_0) - Z_{12}Z_{21}} \quad (\text{S32})$$

where Z_0 is the impedance of the lumped port, which is 50Ω in this case.

In precomputation, a G_{obj} matrix is found for the simulation environment for the end-sections. This matrix maps each current source j at all points in the optimization region to the complex transmission and reflection coefficients (i.e. α_{A2} and β_{A2} for segment A) at the waveguide interface, as well as the field quantities needed to find the voltage and current of the lumped port. This allows the components of the A matrix to be updated at each optimization iteration without field simulation. This is then utilized to compute the objective function from the S-parameters.

Supplementary figures

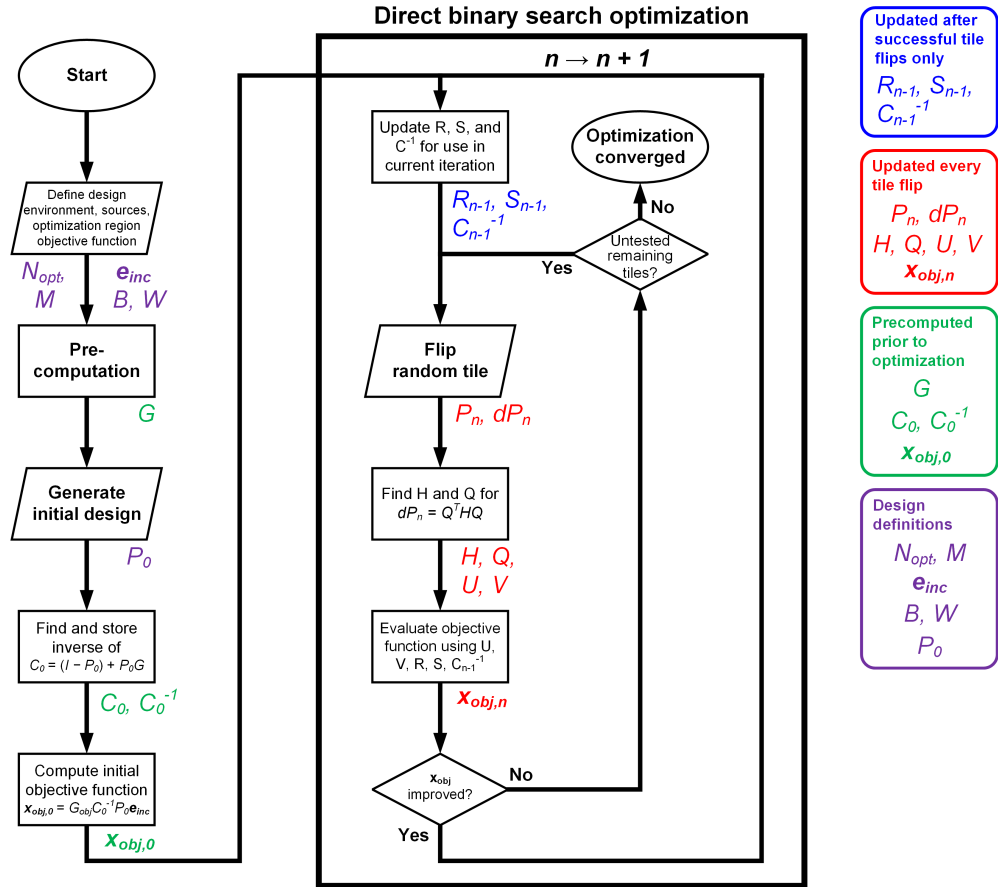


Fig. SF1: Flowchart of inverse design utilizing the precomputed numerical Green function method with direct binary search optimization. Quantities that are determined in each step are indicated, illustrating the reduction in the computation required for optimization via precomputation and the low-rank update technique.

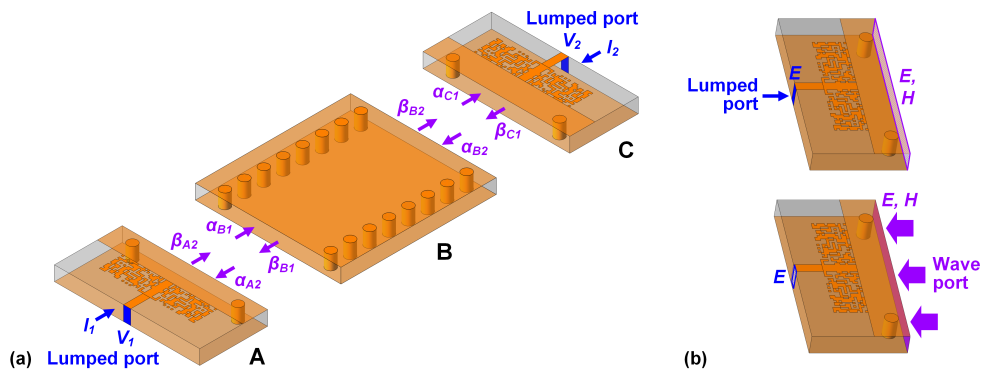


Fig. SF2: Accelerated simulation of waveguide transition structure. (a) Splitting of the microstrip-SIW-microstrip structure into three segments: the waveguide and two transition segments; (b) Illustration of the two field simulations necessary to compute S_{21} . Dimensions and features shown are not to scale. While a microstrip-SIW-microstrip transition is depicted, this technique is applicable to any finite-length waveguide with transitions to feeds at the ends